Research

Comparison of microstructure, mechanical, and electrochemical performance of laser-deposited FeCrV15 alloy at varying powder feed rates

Basiru Philip Aramide[1,3] · Taoreed Adesola Adegbola[1] · Tamba Jamiru[1] · Abimbola Patricia Idowu Popoola[2] ·
Mathew Olurotimi Adeoti[1,4] · Rotimi Emmanuel Sadiku[2]

Abstract
In the realm of surface modification, repair, and reinforcement of components exposed to challenging operational conditions, such as tillage tools, laser cladding stands out as an innovative manufacturing technique. Employing this additive manufacturing approach, a functionally graded material with outstanding strength and properties is incorporated to enhance the desired attributes of the base material. This comparative investigation scrutinized and assessed the microstructural characteristics, hardness, wear resistance, and corrosion behavior of high carbon ferrochrome *FeCrV15* coatings fabricated at two distinct powder feed rates, namely 5 and 6 g/min, respectively. The analysis delved into how the resultant coatings' molten bead deposition, microstructural evolution, hardness, wear resistance, and corrosion resistance were influenced by the powder feed rate. Evaluation of hardness was conducted using a Vickers microhardness testing apparatus, while phase identification was accomplished utilizing an X-ray diffractometer. The morphologies of the microstructures were scrutinized employing optical microscopy and scanning electron microscopy coupled with energy dispersive spectroscopy (SEM/EDS). Furthermore, the corrosion response of the deposits in a soil–water environment was probed utilizing an Autolab potentiostat. A comprehensive assessment of the coatings' sliding wear performance was undertaken using an Anton Paar Tribometer. The findings of the study reveal that an escalation in the powder feed rate engenders heightened grain refinement within the microstructure, yielding a defect-free sample and augmenting the wear performance (with a wear rate of 2.42×10^{-6} mm^3/N/m for sample B, surpassing 2.39×10^{-5} mm^3/N/m for sample A and outstripping 1.72×10^{-3} mm^3/N/m for the steel substrate). Additionally, the corrosion resistance is enhanced (with a corrosion rate of 0.0032 mm/yr for sample B, surpassing 0.0036 mm/yr for sample A, which, in turn, exceeds 0.1168 mm/yr for the steel substrate) in the case of sample B.

Article Highlights

- High-carbon *FeCrV15* coatings were laser-deposited onto steel baseplates using a 3 kW CW IPG Fiber laser system, with two powder feed rates tested.
- The impact of varied powder feed rates on microstructure, mechanical, and electrochemical properties was examined and compared.

✉ Basiru Philip Aramide, abashiruphilip@gmail.com; AramideBP@tut.ac.za | [1]Deptartment of Mechanical and Mechatronics Engineering, Tshwane University Technology, Pretoria, South Africa. [2]Department of Chemical, Metallurgical and Material Engineering, Tshwane University Technology, Pretoria, South Africa. [3]Department of Agricultural and Environmental Engineering, Obafemi Awolowo University, Ile-Ife, Nigeria. [4]Department of Mechanical Engineering, The Federal Polytechnic, Bida, Niger, Nigeria.

○ Discover

- A feed rate of 6 g/min resulted in better wear and corrosion resistance by promoting intermittent M_7C_3 precipitate formation and microstructure enhancement.

1 Introduction

High carbon ferrochrome alloy is in the group of high Cr typecast irons amalgam described by the ASTM A532 as an amalgam belonging to the ternary system of *Fe-Cr-C* with roughly 15–30 wt% *Cr*, 2.4–4 wt% C with some other elements in minor quantity [1–4]. Some high carbon ferrochrome alloys contain other hard elements in high quantity, such as vanadium (roughly 15 wt%); such have a quaternary system of *Fe-Cr-V-C*. This has been used to produce in-situ vanadium-chromium-iron carbides overlay on steel baseplates for mining and tillage applications [5, 6]. The combination of hard carbides incongruent with the relatively mild matrix around it, with averagely low cost and abundant availability [7–9], makes *FeCrV15* alloy an attractive tool-making material in these industries. According to Nayak et al. [1], increasing the chromium content of an iron-base alloy alters the nature and type of carbides formed in the eutectic matrix to an M_7C_3, a discontinuous type, from a continuous M_3C carbide [10, 11]. The authors stressed that the continuous M_3C is associated with inherent brittleness, making it less preferred for abrasion resistance [12]. However, the percentage precipitation, orientation, and grain refinement of the carbides in the microstructure [6] and the closer collaboration of the carbide and the matrix surrounding it determines the overall wear and corrosion resistance [13–15]. Despite the precipitated carbides' indispensable involvement in generally enhancing the wear opposition of iron-base alloys, the degree of structural support provided by the matrix structure is pivotal for wear opposition [16, 17].

Extensive experimentation by researchers has yielded promising results in their quest to improve the durability of equipment regularly subjected to harsh conditions. By combining chromium carbide with vanadium carbide, wear and corrosion resistance in iron-based coatings has been significantly enhanced [18]. The introduction of this structural support has led to a reduced wear rate, effectively extending the lifespan of tools exposed to abrasive and impact-based environments. The primary VCs, eutectic VCs, and Cr-rich eutectic carbides continue to provide effective protection against grinding media [5, 19, 20]. They contribute to improving grain refinement, which results in high toughness and improved wear resistance [6]. One method for depositing these carbides on the surfaces of the tools is laser additive manufacturing technology (laser cladding).

The benefits of laser cladding encompass minimal stress distortion and a narrow heat-affected zone (HAZ), along with shallow and limited dilution ratios, fostering an improved metallurgical bond between the coating and substrate. By enabling precise monitoring and regulation of both the HAZ and power input onto the material, this technique enhances material strength through controlled crystallization rates—an essential factor determining microstructural and mechanical properties [21]. Given that conventional high-temperature welding methods, which are harsh on materials, are presently employed for tool refurbishment and repair, laser cladding holds a competitive advantage over alternatives such as gas metal arc welding (GMAW), submerged arc welding (SAW), and similar techniques.

Aramide et al. [5] explored the influence of chromium-vanadium carbide on the microstructural development and hardness of laser-deposited coatings on steel baseplates. They examined the effects of varying laser beam power and scanning speed (with a constant powder flow rate) on the evolution of coating microstructure, observing significant improvements in both hardness and microstructural features. In another study, Aramide et al. [6] investigated the impact of additional chromium content on the mechanical behavior of *FeCrV15* laser coatings. They noted reduced carbide precipitation, increased coarse grain formation in the microstructure, decreased hardness, and higher corrosion rates in *FeCrV15 + Cr* coatings compared to *FeCrV15* coatings lacking additional chromium. Akinlabi and Akinlabi [22] studied the influence of powder feed rate variation on metal deposits produced by a *TiC* laser on a *Ti6Al4V* substrate. They found that increasing the powder feed rate led to increased defects, improved hardness, and reduced grain size. This study investigates how different powder feed rates impact various aspects of laser-deposited coatings made from high-carbon ferrochrome *FeCrV15*. While past research has focused on factors like laser power and scanning speed [23, 24], this study uniquely emphasizes the importance of the powder feed rate on microstructure formation, mechanical behavior, and electrochemical performance of composite coatings, making a significant contribution to the field.

2 Materials and methods

High carbon ferrochrome *FeCrV15* coatings, produced via laser deposition with a powder distribution of − 150 + 50 µm, were applied onto steel baseplates using a 3 kW Continuous Wave (CW) IPG Fiber laser system, along with a DPSF-21 type coaxial powder feeder. Argon gas, utilized as both shielding and carrying gas, flowed at rates of 15 L/min and 2 L/min, respectively, within the powder feeder. The deposition process involved the creation of five coating tracks with 50% overlaps, resulting in three coating layers. This experimental procedure was repeated three times for reliability. The SEM micrograph depicting the powder is presented in Figs. 1, 2 presents CW IPG Fiber laser system, while Table 1 provides the weight composition of the powder and baseplate. Additionally, Table 2 outlines the manufacturing parameters of the samples along with their definitions.

The samples underwent meticulous preparation, involving grinding and polishing using silicon carbide paper of various coarseness levels, namely 80, 380, 1200, and 1400 grit sandpapers, to achieve a smooth surface before microstructural examination. Subsequently, the test surfaces underwent further polishing to achieve a reflective finish. Etching of the finished samples' surfaces was performed using a modified version of Fry's Reagent composed of 150 ml H_2O, 50 ml HCl, 25 ml HNO_3, and 1 g $CuCl_2$. Microstructural analysis was conducted utilizing an optical polarizing microscope (OPM) and

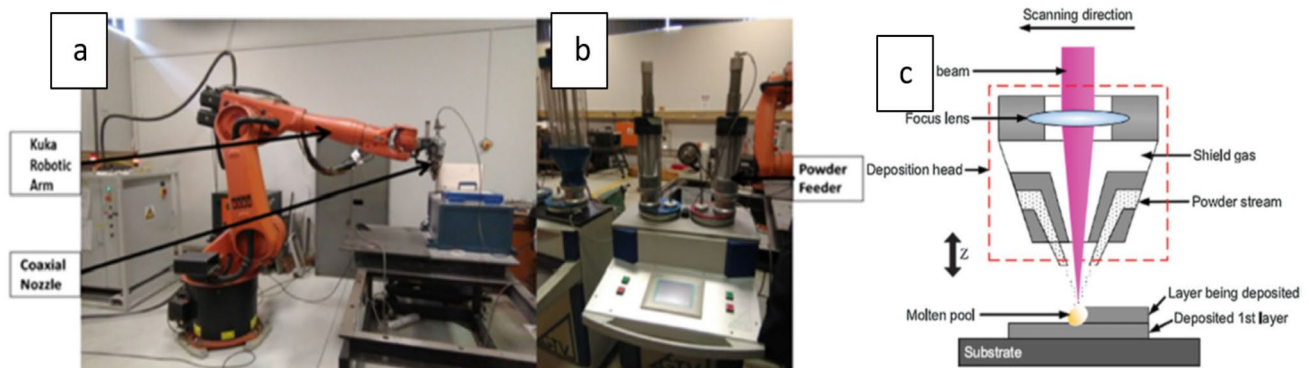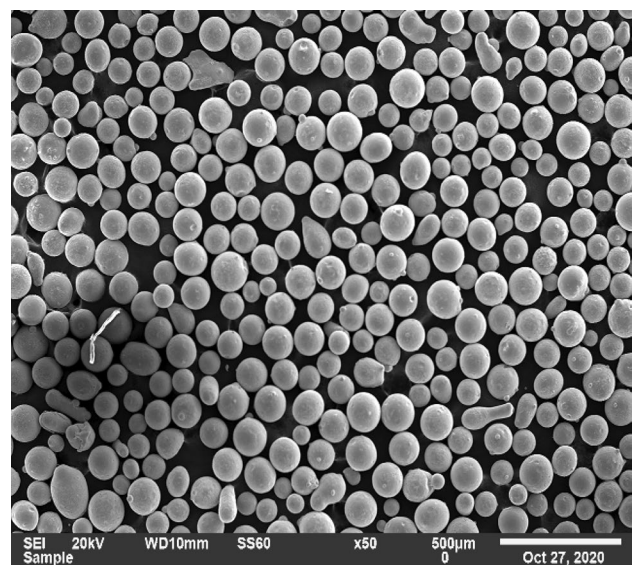**Fig. 1** The micrograph of high carbon ferrochrome powder

Fig. 2 The IPG fiber laser setup (**a**), powder dispenser (**b**), and the illustrative diagram showcasing the laser head (**c**).

Table 1 The elemental weight configuration of the powder and the base plate

Elements	C	Mo	Mn	O	Cr	Si	V	Al	Fe
FeCrV15	4.5	1.3	1.1	–	14.0	1.1	15.4	–	Balance
Baseplate	2.54	–	1.32	–	–	0.12	–	0.17	Balance

	Samples	Laser Beam power (W)	Scanning speed (mm/s)	Powder used	Powder feed rate (g/min)
Table 2 The samples, depositing powders and their manufacturing parameters	A	1200	8	FeCrV15	5
	B	1200	8	FeCrV15	6

a scanning electron microscope equipped with energy-dispersive spectroscopy (SEM/EDS). Additionally, X-ray diffraction analysis was performed using an X-ray diffractometer with Cu radiation and a parallel beam of 2 mm diameter. The hardness profile of the coatings was assessed using a fully automated FM-ARS900 Vickers testing equipment (Future-Tech Corp., Kanagawa, Japan), applying a load of 300 g dispersed over 200 µm from the top of the coating to the center of the substrates.

The wear experiment was conducted using an Anton Paar Tribometer, with the objective of determining wear rates and friction coefficients (COF). A silicon nitride ball with a radius of 1.5 mm was employed for this purpose. The experimental parameters included a 10 N load, a speed of 200 rpm, and a duration of 15 min. Wear rate evaluation was performed using a profilometer to profile the wear track.

For the electrochemical polarization study, an automated Autolab Potentiostat (PGSTAT302) was utilized. The experiment was carried out in a three-electrode cell configuration, where the samples served as working electrodes with an exposed surface area of 100 mm^2. The reference electrode employed was AgCl/Ag, while a platinum electrode functioned as the counter electrode. Upon attaining system stability, the open-circuit potential was measured, followed by polarization tests to maintain a consistent potential at a scan rate of 1 mV/s. This methodology was implemented using a soil water solution derived from typical agricultural soil and conducted under ambient temperature conditions.

3 Experimental results and analysis

The SEM images depicting samples A and B are showcased in Fig. 3. In these images, dark precipitates have been discerned and designated as vanadium carbides (VCs) (position 1), while the grey or whitish lamellar phase corresponds to the amalgamation of iron, eutectic VCs, and Cr-rich carbides (position 2). Additionally, the dark grey region represents the martensite and austenite phase (position 3) [5, 20].

In sample A, the precipitation of vanadium carbides (VCs) exhibited star-like formations characterized by larger grains and lower percentage concentrations compared to sample B. Conversely, sample B demonstrated enhanced grain refinement and higher percentage concentrations of the precipitated carbides, as illustrated in Fig. 3. The comprehensive elemental compositions of both samples are detailed in Table 3, as per the overall Energy Dispersive Spectroscopy (EDS) analysis results. Furthermore, X-ray Diffraction (XRD) diffractometric analysis results, depicted in Fig. 4, substantiate the in-situ formation of carbides within the deposited coatings, as previously mentioned.

3.1 The effect of the powder feed rate on the melt bead features

Samples A and B denote the coatings fabricated from *FeCrV15* powder, utilizing identical laser-beam power and scanning speed parameters but employing distinct powder feed rates (PFR) of 5 g/min and 6 g/min, respectively, as delineated in Table 2. The experimental findings reveal the presence of defects and pores in sample A, accompanied by a notably high heat-affected zone and a prominent dilution ratio, as illustrated in Fig. 5A. In contrast, sample B exhibits a defect-free surface with minimal dilution and a reduced heat-affected zone, as depicted in Fig. 5B. The graphical representation of the dilution ratio is presented in Fig. 5C, where the dilution ratio for sample A approximates 18%, whereas for sample B, it stands at approximately 0% [5, 20]

$$Dilution\ Rate\ [\%] = \frac{A_E}{A_E + A_A} * 100$$

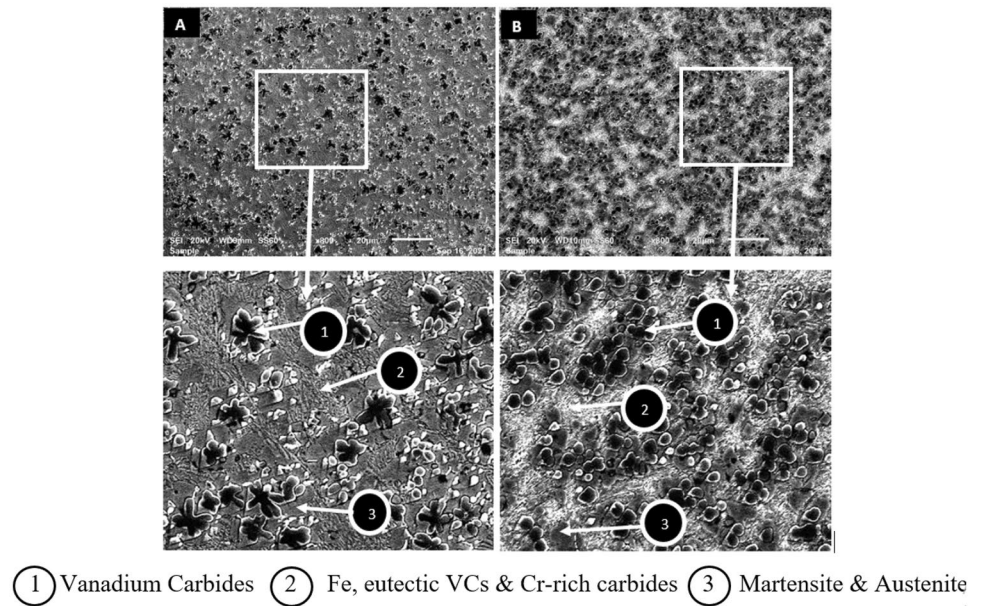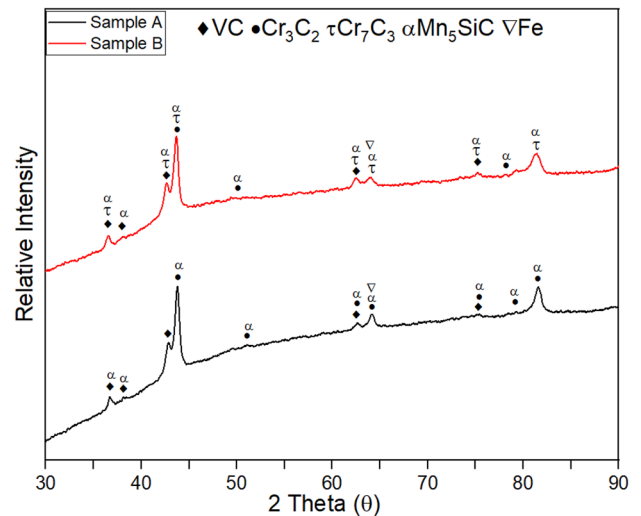**Fig. 3** SEM image showing the microstructure **A** sample A, **B** sample B

① Vanadium Carbides   ② Fe, eutectic VCs & Cr-rich carbides   ③ Martensite & Austenite

Table 3 The overall EDS measurement of both samples in wt%

Samples\Element	C K	O K	Si K	V K	Cr K	Fe K	Mn K	Mo K
A	11.16	0.00	0.96	14.28	10.55	61.07	0.84	1.14
B	6.31	0.00	1.02	19.08	15.10	56.30	1.31	0.11

Fig. 4 XRD Plot of the coatings

3.2 The effect of the powder feed rate on the microstructures of the clad

In Sample A, the reduction in Powder Feed Rate (PFR) resulted in a diminished concentration of elements from the powder, accompanied by an increased specific heat input per unit mass of the molten pool (comprising both powder and substrate). Consequently, this discrepancy led to a higher dilution ratio in comparison to Sample B (as illustrated in Fig. 5A). The relatively elevated specific heat input per unit mass of the powdered constituents in Sample A facilitated the formation of star-like aggregations and the precipitation of Vanadium Carbides (VCs) with increasing depth into the clads (as depicted in Figs. 3A, 6A, 7A, B, C).

Fig. 5 Effect of powder flow rate on the melt bead features, sample A developed with 5 g/min PFR has pores and defects (**A**), sample B developed with 6 g/min PFR exhibits a defect free surface (**B**), and a representation of dilution ratio (**C**)

$$\text{Dilution Rate } [\%] = \frac{A_E}{A_E + A_A} * 100$$
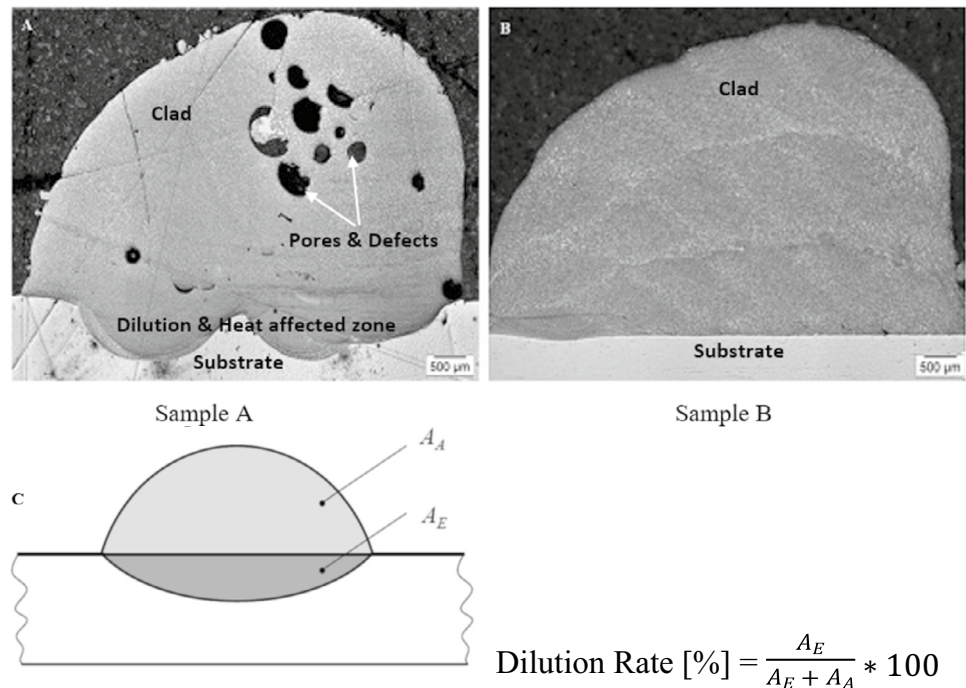
Conversely, in Sample B, the higher PFR resulted in a lower specific heat input per unit mass of the molten pool of powdered constituents, thereby preserving the spherical morphology of VCs throughout the microstructure (as shown in Figs. 3B, 6B, 7D–F). Within Sample A, carbide precipitates underwent partial or complete melting within the microstructure due to the elevated specific heat input, consequently diminishing their resistance to abrasive wear. This phenomenon also elucidates the observed morphologies assumed by the precipitated carbides.

In contrast, carbide precipitates in Sample B remained unmelted, a characteristic believed to contribute to its reinforcement and enhancement of hardness, thereby augmenting its resistance against abrasive wear.

Furthermore, a meticulous analysis of the micrographs depicted in Fig. 7 reveals discernible alterations in the phase distribution as one progresses deeper into the clad, utilizing the substrate as the point of reference [5, 19]. The precipitation of eutectic carbides, incorporating vanadium carbides (VCs), iron, and chromium-rich phases, was discerned as whitish-grey regions enveloped by dark martensitic phases distributed across the micrograph. The agglomeration and genesis of primary VCs were noted to commence, exhibiting an average diameter of 0.69 μm, enclosed by dark martensitic phases roughly 500 μm distant from the substrate (refer to Fig. 7A) [5]. The molten vanadium carbides (VCs) exhibited further aggregation, resulting in the formation of star-shaped configurations of primary VCs, measuring approximately 2.55 μm in diameter, located at a depth of approximately 900 μm into the cladding for sample A. Moreover, a comparable trend of augmented carbide grain size with distance into the cladding was noted in sample B (refer to Fig. 7D–F).

Fig. 6 Sample A's star-like microstructural precipitation (**A**), and sample B's rounded precipitates of primary VCs (**B**) [25]
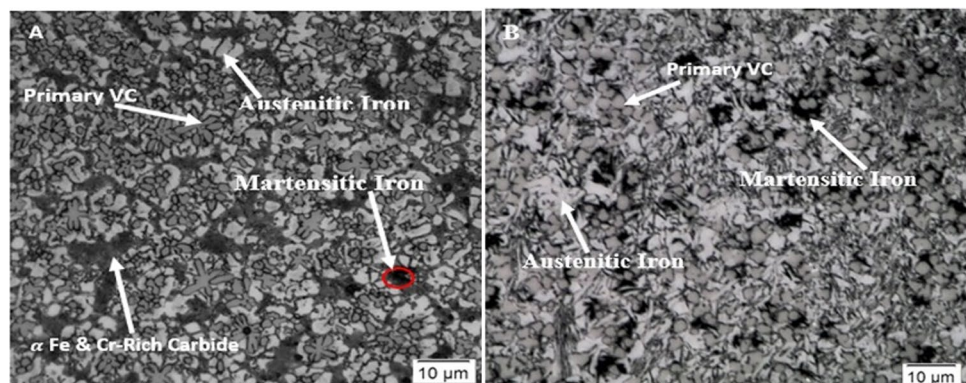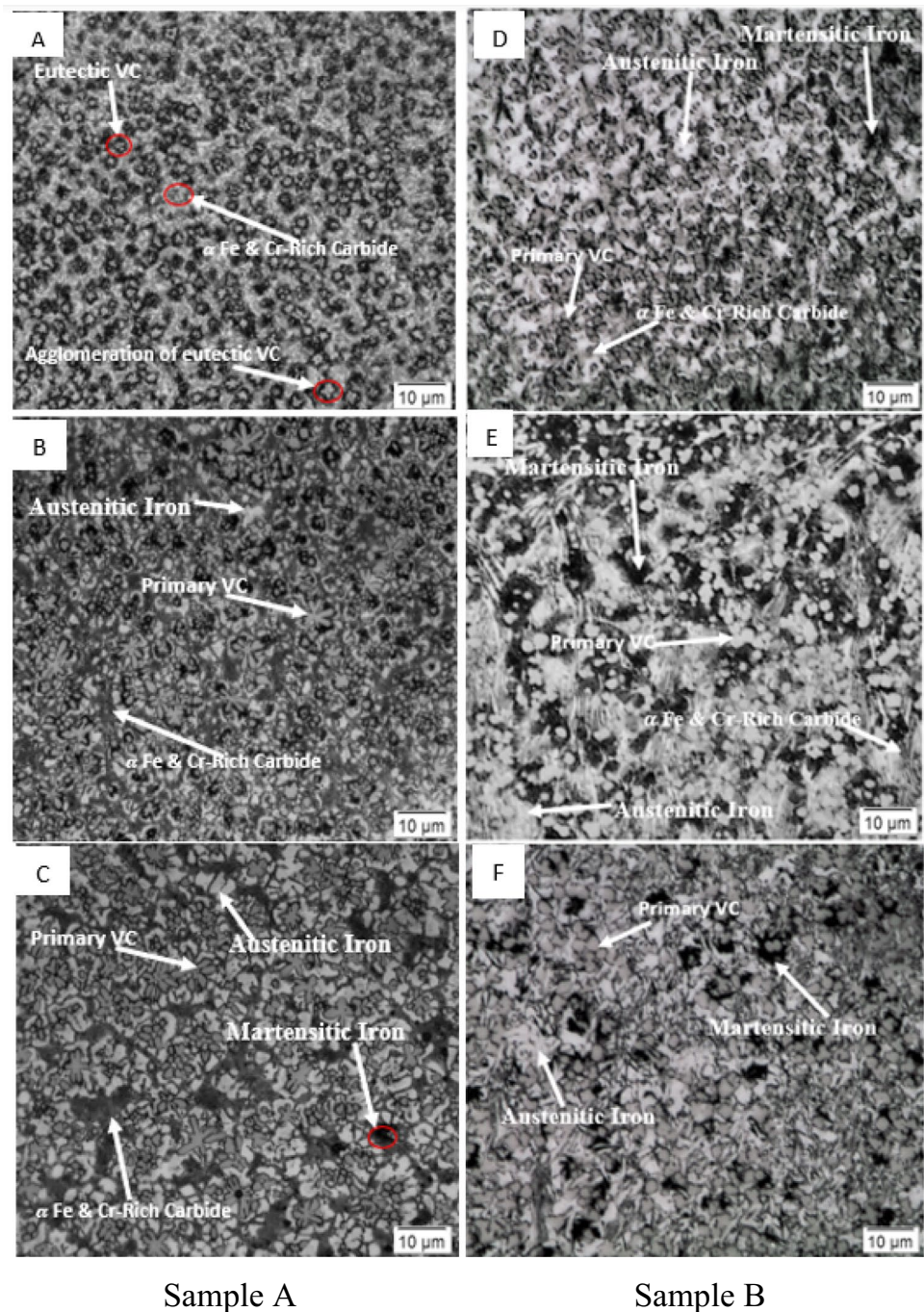
Fig. 7 The OPM images of the samples at different depth into the clads, (**A**, **B**, and **C**) for sample A, (**D**, **E** and **F**) for sample B

Sample A   Sample B

3.3 The microhardness of the coatings

The hardness and mechanical characteristics of the developed coatings are influenced by several factors, including the percentage concentration of precipitated carbide phases [26, 27], the arrangement or refinement of grain and its boundaries [28], and the synergistic interaction between the carbide and the surrounding matrix in the microstructure [13–17]. Hardness measurements were conducted both longitudinally and transversely across the samples, at intervals of 200 µm, using a load of 300 g and a dwell time of 10 s. The average hardness observed for samples A and B was 835 HV 0.3 and 1000 HV 0.3, respectively, while the substrate had 170 HV 0.3. As mentioned earlier, the hardness profiles of the coatings were also taken; Fig. 8 represents the hardness profiles of both samples. The higher microhardness values of coatings
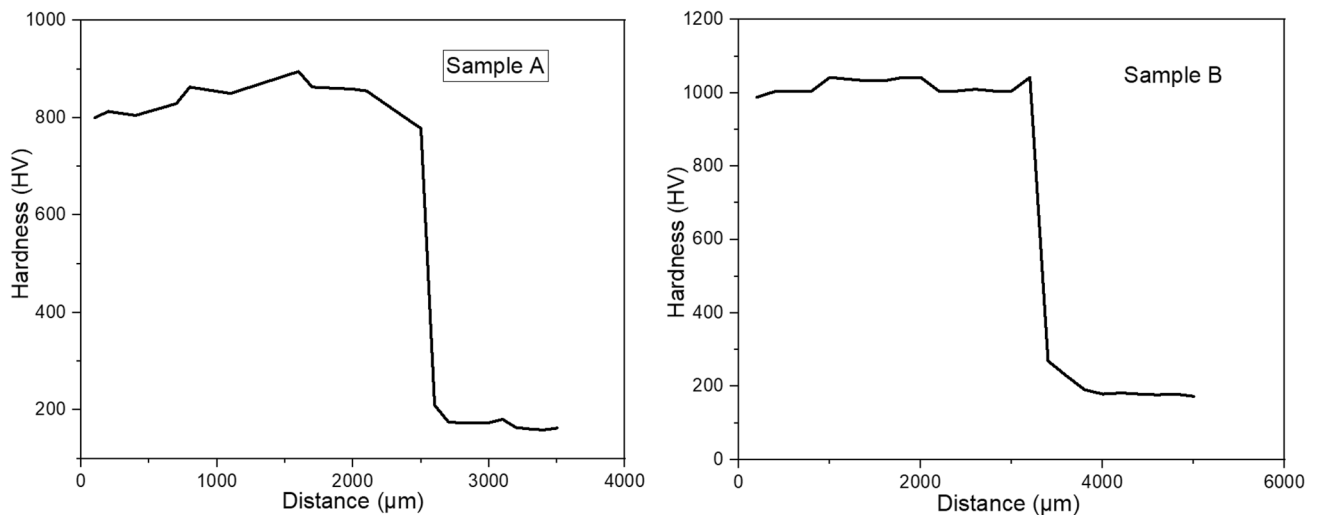
Fig. 8 The hardness profile of the samples

Table 4 Wear rate for control and the coatings	Samples	Material	Wear rate (mm³/N/m)
	Control	EN48 Steel	1.72×10^{-3}
	A	FeCrV15-5	2.39×10^{-5}
	B	FeCrV15-6	2.42×10^{-6}

compared to the substrate could be explained by the precipitation of hard VC-Cr_3C_2 in sample A and VC-Cr_3C_2-Cr_7C_3 in sample B; the XRD results confirm this. Increasing the powder feed rate increases the volume of vanadium, chromium, carbon, etc., in the microstructure of sample B, which explains the additional precipitation of the discontinuous M_7C_3 and better grain refinement in this coating than in sample A.

Produced using a lower PFR, Sample A displayed hardness profiles affected by melted carbide precipitates within its microstructure. The star-like configurations of vanadium carbides (VCs) in Sample A, featuring larger grains and lower percentage concentrations than those in Sample B, resulted in diverse hardness profiles throughout the coating thickness. However, Sample B, produced with a higher PFR, displayed hardness profiles characterized by intact/unmelted carbide precipitates throughout the microstructure. The enhanced grain refinement and higher percentage concentrations of precipitated carbides in Sample B resulted in more uniform and higher hardness profiles across the coating thickness compared to Sample A.

3.4 The wear characteristic of the coatings

The sliding wear test conducted on the substrate and the samples at ambient temperature is presented in Table 4, along with Figs. 9 and 10. Notably, Sample B exhibits superior wear resistance compared to Sample A, as evidenced by its notably higher wear resistance and lower wear rate. Specifically, Sample B demonstrates a wear resistance approximately tenfold greater than that of Sample A. Moreover, both coatings display significantly enhanced wear resistance compared to the substrate [29], as illustrated in Fig. 9 and detailed in Table 4. The disparities in the coefficient of friction (COF) over time, depicted in Fig. 10, elucidate the observed differences in wear resistance between the samples. Sample B manifests a relatively consistent COF curve, commencing at approximately 0.41, maintaining a steady trajectory, and concluding at a similar value. Conversely, Sample A exhibits a fluctuating COF curve, starting with a substantially higher COF of ~0.48 and following an irregular pattern before reaching ~0.39. This notable initial COF value [30, 31], coupled with its erratic behavior, elucidates the lower wear resistance observed in Sample A.

Moreover, the mechanical properties of Sample A were possibly compromised due to the varying hardness profiles stemming from the presence of melted carbide precipitates. The partial or complete melting of these carbide precipitates reduced their ability to resist abrasive wear, consequently impacting the coating's overall durability and performance.

Fig. 9 The control and the coatings' wear rate
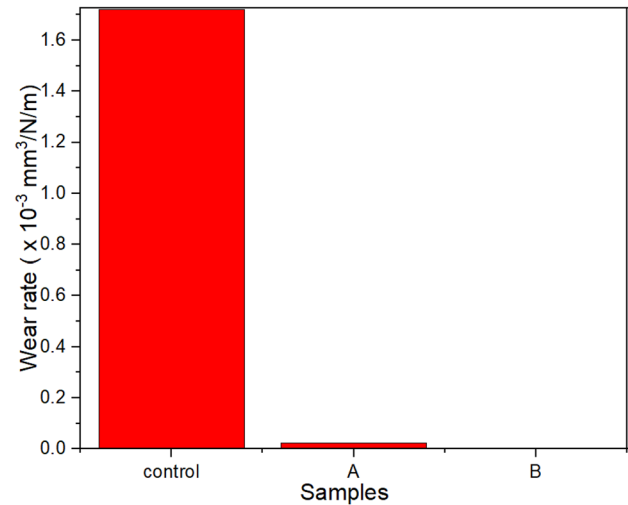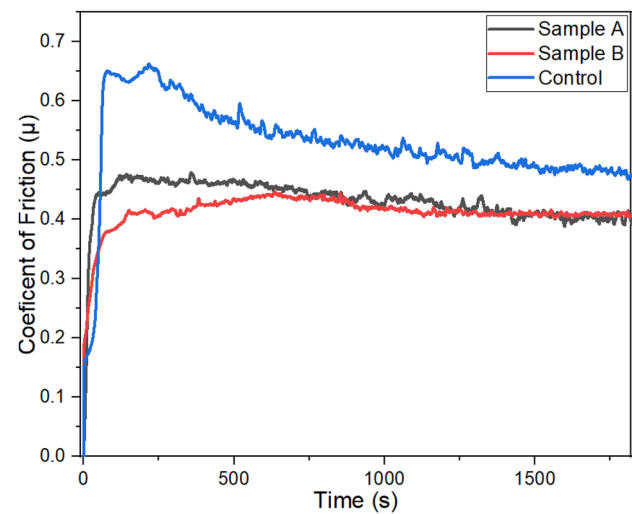

**Fig. 10** The coatings' friction coefficient

In contrast, Sample B showcased enhanced mechanical properties relative to Sample A, attributed to intact carbide precipitates and more uniform hardness profiles. The retention of carbide precipitates, along with improved grain refinement, played a vital role in reinforcing the coating and augmenting its resistance to abrasive wear, ultimately bolstering its durability and service life.

3.5 The electrochemical characterisation of the coatings

The polarization curve utilized to assess the corrosion performance of the coatings in a soil–water environment at room temperature is depicted in Fig. 11. The anodic and cathodic polarization curves display uniform patterns throughout their profiles and demonstrate asymmetry, as discernible from their forms. Adhering to Tafel's behavior principles, the anodic segment of the curves portrays the coating's dissolution, while the cathodic segment illustrates hydrogen generation via water molecule reduction. The augmentation of the powder feed rate yielded a heightened formation of carbides within the coatings, consequently enhancing corrosion resistance by diminishing the corrosion current density (Icorr) and elevating the corrosion potential (Ecorr). These observations underscore the inhibitory characteristics of the deposited coatings, which establish a protective barrier, impeding corrosion mechanisms and thereby augmenting the coating's resistance to corrosion [32]. Upon inspection, it is evident that the curve for Sample B shifts marginally towards the anodic region with Ecorr value of − 0.54698 and Icorr of 2.83E−07, whereas Sample A shifts towards the cathodic region of the potential with Ecorr value of − 0.57776 and Icorr of 3.13E−07. This shift suggests that Sample B exhibits superior corrosion resistance compared to Sample A. The corrosion parameters of the coatings are detailed in Table 5, where it is observed

Discover

Fig. 11 The polarisation curve of the coatings
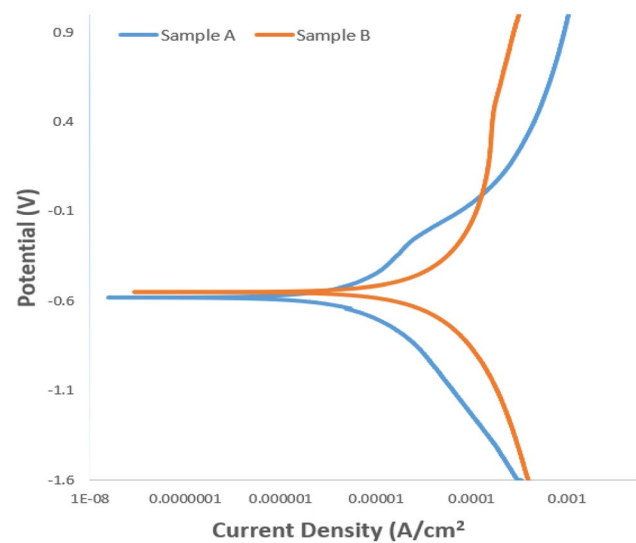
that the corrosion rate increases proportionally with the corrosion current density. Specifically, Sample A, fabricated with a powder feed rate of 5 g/min, exhibits a higher corrosion rate of 0.0036 mm/year, whereas Sample B demonstrates a lower rate of 0.0032 mm/year. The augmentation of the powder feed rate leads to the formation of discontinuous M_7C_3 carbides and enhances the grain refinement of the coating's microstructure. Consequently, this fosters favorable conditions for the development of a passive film, resulting in reduced corrosion rates observed in Sample B [33–35].

4 Conclusion

Laser-deposited high carbon ferrochrome *FeCrV15* coatings were made on steel baseplates with two different powder feed rates using a 3 kW Continuous Wave (CW) IPG Fibre laser system. The impact of the powder feed rate and the laser-specific heat input on the microstructural formation, hardness, wear and corrosion performance of the coatings were investigated, and the following outcomes were observed:

- Pores and defects were observed in the coating of a lower powder feed rate (sample A) with a high dilution ratio of approximately 18% due to the higher specific heat input on both the powder and substrate. In contrast, sample B is a defect-free coating with a dilution ratio of approximately 0%.
- The precipitation of in-situ *VC-Cr₃C₂* and a hardness value of 835 HV 0.3 was observed in sample A, while in sample B, the formation of *VC-Cr₃C₂-Cr₇C₃* with a hardness value of 1000 HV 0.3 was recorded.
- The higher specific heat input on both individual powder elements and substrate resulted in the star-like formation of carbides with bigger grains in sample A; however, sample B has considerably refined grains of carbides with round moulded shapes.
- Optimal wear and corrosion resistance were observed at 6 g/min powder feed rate due to discontinuous M_7C_3 precipitates and improved grain refinement.
- The variation in powder feed rate impacted the hardness profiles of the coatings, resulting in distinct mechanical property variations between samples A and B. Sample B, characterized by preserved carbide precipitates and consistent

Table 5 Potentiodynamic polarisation tafel data

Samples	Powder feed rate (mm/s)	E_{corr} (V)	I_{c0rr} (A/cm^2)	Corrosion rate (mm/yr)
A	5	− 0.57776	3.13E−07	0.003632
B	6	− 0.54698	2.83E−07	0.003288
Control	–	− 0.71087	1.00E−05	0.1168

hardness profiles, exhibited enhanced mechanical characteristics in contrast to Sample A. In Sample A, where carbide precipitates experienced partial or complete melting, the mechanical integrity and performance were compromised.

Data availability The raw/processed data required to reproduce these findings cannot be shared at this time as the data also forms part of an ongoing study.

Declarations

Competing interests The authors assert that they possess no identifiable conflicting financial interests or personal relationships that might have seemed to impact the findings presented in this paper.

References

1. Nayak UP, et al. Load dependent microstructural evolution in an as-cast 26% Cr high chromium cast iron during unlubricated sliding. Friction. 2021;10(8):1258–75. https://doi.org/10.1007/s40544-021-0553-x.
2. Tabrett CP, Sare I, Ghomashchi M. Microstructure-property relationships in high chromium white iron alloys. Int Mater Rev. 1996;41(2):59–82.
3. Nayak UP, Guitar MA, Mücklich F. A comparative study on the influence of chromium on the phase fraction and elemental distribution in as-cast high chromium cast irons: simulation vs experimentation. Metals. 2020;10(1):30.
4. ASTM International. Standard Specifications for Abrasion Resistance Cast Iron: ASTM Standard A 532/A 532M-93a. . West Conshohocken, PA, USA, 2003.
5. Aramide B et al. Influence of vanadium-chromium carbide on the microstructure of reinforced FeCrV15 hardfacing during laser cladding deposit. J Mater Eng Perform. 2021; 31(1): 514–523.
6. Aramide B, et al. Influence of extra chromium addition on the microstructure, hardness, and corrosion behaviour of high carbon ferro-chrome FeCrV15 deposited through laser cladding on steel baseplate for tillage application. Surf Topogr Metrol Prop. 2021;9(4): 045029.
7. Aramide B, et al. Improving the durability of tillage tools through surface modification—a review. Int J Adv Manuf Technol. 2021;116(1):83–98.
8. Gu J, et al. Microstructure and wear behavior of laser cladded Ni45 + high-carbon ferrochrome composite coatings. Materials. 2020;13(7):1611.
9. Zhang H, et al. Effects of CeO2 on microstructure and corrosion resistance of TiC-VC reinforced Fe-based laser cladding layers. J Rare Earths. 2014;32(11):1095–100.
10. Rivlin V. 14: Critical review of constitution of carbon—chromium—iron and carbon—iron—manganese systems. Int Metals Rev. 1984;29(1):299–328.
11. Maratray F, Usseglio-Nanot R. Factors affecting the structure of chromium and chromium–molybdenum white irons. 1970.
12. Pearce J. Structure and wear performance of abrasion resistant chromium white cast irons (Retroactive Coverage). Trans Am Foundrymen's Soci. 1984;92:599–622.
13. Doğan Ö, Hawk J. Effect of carbide orientation on abrasion of high Cr white cast iron. Wear. 1995;189(1–2):136–42.
14. Wiengmoon A. Carbides in high chromium cast irons. Naresuan Univ Eng J. 2011;6(1):64–71.
15. Wiengmoon A, Pearce JTH, Chairuangsri T. Relationship between microstructure, hardness and corrosion resistance in 20wt%Cr, 27wt%Cr and 36wt%Cr high chromium cast irons. Mater Chem Phys. 2011;125(3):739–48.
16. Laird G, Gundlach RB, Röhrig KK. Abrasion-resistant cast iron handbook. 2000: American Foundry Society.
17. Avery HS. The measurement of wear resistance. Wear. 1961;4(6):427–49.

18. Aramide BP, et al. Mechanical, wear and corrosion behaviours of laser additive manufactured iron-based heterogeneous composite coatings for tillage tools. Results Surf Interfaces. 2024;15: 100214.
19. Aramide BP et al. Influence of vanadium-chromium carbide on the microstructure of reinforced FeCrV15 hardfacing during laser cladding deposit. Res Square, 2021.
20. Günther K, Bergmann JP. Influencing microstructure of vanadium carbide reinforced FeCrVC hardfacing during gas metal arc welding. Metals. 2020;10(10):1345.
21. Vilar R. Laser cladding. J Laser Appl. 1999;11(2):64–79.
22. Akinlabi ET, Akinlabi SA. Powder flow rate influence on laser metal deposited TiC on Ti-6Al-4V. no Lmd. 2016.
23. Aramide B, et al. Scanning speed effect on the microstructure, hardness, wear, and corrosion performance of VC-Cr3C2 reinforced laser claddings on steel baseplate for tillage application. Trans Indian Inst Metals. 2022. https://doi.org/10.1007/s12666-022-02587-5.
24. Aramide B, et al. The microstructure and anti-wear property of FeCrV15 and FeCrV15+Cr deposits fabricated via laser deposition on steel base-plate for soil-working tools. Appl Phys A. 2022;128(6):490.
25. Aramide B, et al. Effect of powder flowrate on the microstructure of FeCrV15 clad, developed via the laser cladding technique. Mater Today Proc. 2022. https://doi.org/10.1016/j.matpr.2022.02.093.
26. Kocaman E, et al. The influence of chromium content on wear and corrosion behavior of surface alloyed steel with Fe(16–x)Crx(B, C)4 electrode. Eng Sci Technol Int J. 2021;24(2):533–42.
27. Venkatesh B, Sriker K, Prabhakar VSV. Wear characteristics of hardfacing alloys: state-of-the-art. Proc Mater Sci. 2015;10:527–32.
28. Ralston KD, Birbilis N. Effect of grain size on corrosion: a review. Corrosion. 2010;66(7):075005–075005-13.
29. Bharat N, Bose PSC. Influence of nano-TiO2 particles on the microstructure, mechanical and wear behaviour of AA7178 alloy matrix fabricated by stir casting technique. Proc Inst Mech Eng Part L J Mater Des Appl. 2022;237(4):753–66.
30. Bharat N, Bose PSC. Microstructure, texture, and mechanical properties analysis of novel AA7178/SiC nanocomposites. Ceram Int. 2023;49(12):20637–50.
31. Ramesh CS, et al. Friction and wear behavior of Ni–P coated Si3N4 reinforced Al6061 composites. Tribol Int. 2010;43(3):623–34.
32. Bharat N, Bose PSC. Nano SiC-reinforced AA7178 matrix alloy: corrosion behavior and characterization. SILICON. 2024;16(4):1627–34.
33. Fattah-alhosseini A, Vafaeian S. Comparison of electrochemical behavior between coarse-grained and fine-grained AISI 430 ferritic stainless steel by Mott-Schottky analysis and EIS measurements. J Alloy Compd. 2015;639:301–7.
34. Dada M, et al. The comparative study of the microstructural and corrosion behaviour of laser-deposited high entropy alloys. J Alloy Compd. 2021;866: 158777.
35. Fattah-alhosseini A, et al. The semiconducting properties of passive films formed on AISI 316 L and AISI 321 stainless steels: a test of the point defect model (PDM). Corros Sci. 2011;53(10):3186–92.